

Validation of a novel coupled orbit-attitude propagator by comparison to SLR data and light curves

Luc B. M. Sagnières^{1,2}, Inna Sharf¹, and Florent Deleflie²

¹Department of Mechanical Engineering, McGill University, Montreal, Quebec, Canada

²IMCCE, Observatoire de Paris, PSL Research University, Paris, France

Abstract

Accurate knowledge of the rotational dynamics of a large space debris is crucial for the success of an eventual active debris removal mission charged with its stabilization, capture and removal from orbit. In this light, the development of a novel coupled orbit-attitude propagation tool, D-SPOSE (Debris SPin/Orbit Simulation Environment), whose primary goal is the study of the long-term evolution of the attitude dynamics of large space debris, is outlined, with an emphasis on its comprehensiveness and flexibility of operation. The propagator is applied to three passive geodetic satellites for which there exist abundant observations of the evolution of their attitude state: LAGEOS-2, LARES, and Ajisai. A comparison of simulation results with satellite range measurements and photometric measurements is made, confirming the benefit of the presented attitude dynamics model for future application to defunct satellites as part of space debris remediation efforts.

1 Introduction

The space debris population around Earth has been steadily increasing since the beginning of the Space Age. Mitigation efforts have increased in the last two decades and while stopping the trend is crucial for the safety of future space operations, coming back to a stable space environment can only be achieved by removing current debris from orbit [1]. As such, remediation efforts, including Active Debris Removal (ADR) missions, are being developed around the world. These missions consist of the launch of a removal spacecraft which would rendezvous with a large debris target, capture and stabilize it, and finally remove it from orbit, either by burning it in the atmosphere, or by placing it in a disposal orbit [2]. These efforts, however, can only succeed if an accurate estimation of the target's rotational state is obtained prior to launch. Knowing the target's spin parameters is critical for the stabilization and capture stage. In this light, multiple observation campaigns of high-value targets in densely populated orbits are underway [3, 4, 5, 6], and, in parallel, modelling efforts are trying to characterize the long-term evolution of the attitude dynamics of defunct satellites, which, combined, will benefit the understanding and forecasting of the dynamics of these possible targets [7, 8, 9, 10].

D-SPOSE (Debris SPin/Orbit Simulation Environment), the novel propagator described in this work, builds on the model presented in [11]. With a planned public release by the end of 2018, its purpose is to function as a highly flexible and comprehensive coupled orbit-

attitude propagation tool for large defunct satellites in order to study their attitude dynamics and derive a concrete understanding of their long-term evolution. The goal of the present work is to make use of observations of the spin parameters of three passive geodetic satellites still in operation to validate the developed model. Spherical non-attitude-controlled geodetic satellites prove to be ideal candidates for this as observations of their rotational state are abundant - a necessity for geodesy studies - due to the fact that they are equipped with multiple corner cube reflectors (CCRs), facilitating high-repetition rate (kHz) satellite laser ranging (SLR) measurements organized by the International Laser Ranging Service (ILRS) from which attitude estimates can be determined [12, 13, 14, 15]. Moreover, photometric measurements (light curves) leading to further observations of their attitude state can also be obtained when the satellites are illuminated by the Sun [16, 17]. The chosen spacecraft for this study therefore include the American and Italian LAGEOS-2 and Laser Relativity Satellite (LARES), and the Japanese Ajisai satellite.

Previous spin models have already been developed for these satellites, most notably the LageOS Spin Axis Model (LOSSAM) and its recent upgrade, the LArase Satellites Spin mOdel Solutions (LASSOS) model [18, 19]. However, these models were tailored specifically for these geodetic spherical satellites and can not be applied to any generic spacecraft. The development of our propagator fills a gap in ongoing research into the spin dynamics of space debris, with the possibility of being applied to large satellites where any of the multiple torques in-

cluded can manifest itself as the dominant external perturbation.

First, the model behind D-SPOSE will be introduced in Section 2 with an emphasis on the improvements made since the previous version documented in [11] and its differences with LOSSAM and LASSOS. Sections 3-5 will then go through the various case studies, comparing the simulation results for LAGEOS-2, LARES, and Ajisai, respectively, to observations of their spin parameters as identified by SLR and light curves. Finally, a summary of the findings followed by a discussion of future possible model developments will be presented in Section 6.

2 Model Description

As previously mentioned, the model described in this section is a continuation of work previously published which focused on the rotational dynamics of the defunct European environmental satellite Envisat [11]. Section 2.1 will present the necessary dynamics and will build on the previous model by specifying recent modifications that led to the creation of D-SPOSE. Section 2.2 will present the format of the tool with the required input parameters.

2.1 Dynamics

Dealing with satellite dynamics requires an analysis of the six degrees of freedom governing the orbit and attitude of spacecraft. Three vector differential equations describe the evolution of the corresponding variables. First is the dynamics equation for orbital motion in an Earth-centered inertial (ECI) coordinate frame [20]:

$$\ddot{\mathbf{r}}(t) = -\frac{\mu}{r(t)^3}\mathbf{r}(t) + \sum_j \mathbf{a}_j(t, \mathbf{r}(t), \mathbf{v}(t), \mathbf{q}(t), \boldsymbol{\omega}(t)) \quad (1)$$

where \mathbf{r} is the position as a function of time t , $r = \|\mathbf{r}\|$, \mathbf{v} is the velocity, \mathbf{q} is the attitude parametrization, chosen here to be a quaternion, $\mathbf{q} = [q_0 \ \mathbf{q}_v^T]^T$, $\boldsymbol{\omega}$ is the angular velocity of the body with respect to the inertial frame, $\mu = 3986004.418 \times 10^8 \text{ m}^3 \text{ s}^{-1}$ is the Earth's gravitational parameter, and \mathbf{a}_j represents the additional considered accelerations due to orbital perturbations. The specific inertial frame chosen is the True Equator Mean Equinox (TEME) frame of the initial chosen Two-Line Element (TLE) epoch [21].

The second differential equation, the dynamics equation for attitude motion, relates the evolution of absolute angular velocity to the sum of the external torques, $\boldsymbol{\tau}_j$, about the body's center of mass [22]:

$$\mathbf{I}\dot{\boldsymbol{\omega}}(t) + \boldsymbol{\omega}(t) \times \mathbf{I}\boldsymbol{\omega}(t) = \sum_j \boldsymbol{\tau}_j(t, \mathbf{r}(t), \mathbf{v}(t), \mathbf{q}(t), \boldsymbol{\omega}(t)) \quad (2)$$

where \mathbf{I} is the matrix representation of the inertia tensor of the rigid body in the centroidal body-fixed frame.

All vectors in Eq. (2) represent components in the same body-fixed frame; the superscript \times denotes the skew-symmetric matrix representation of the cross-product.

Finally, the third differential equation is the kinematic equation for the absolute orientation of the spacecraft:

$$\dot{\mathbf{q}}(t) = \frac{1}{2}\boldsymbol{\Omega}(\boldsymbol{\omega})\mathbf{q}(t) \quad (3)$$

where, expressed in terms of the body-frame components of $\boldsymbol{\omega}$:

$$\boldsymbol{\Omega} = \begin{bmatrix} 0 & -\omega_x & -\omega_y & -\omega_z \\ \omega_x & 0 & \omega_z & -\omega_y \\ \omega_y & -\omega_z & 0 & \omega_x \\ \omega_z & \omega_y & -\omega_x & 0 \end{bmatrix} \quad (4)$$

In the present work, Equations (1)-(3) are numerically propagated using a fifth-order Runge-Kutta method called the Runge-Kutta Dormand-Prince (RKDP) numerical integration method [23]. The same integration time step is used for propagating Eqs. (1)-(3).

The accelerations and torques due to external perturbations, as well as the environmental models considered, are summarized in Table 1. These include Earth's gravitational acceleration due to its deviation from that of a homogeneous sphere, the gravity-gradient torque, and third-body gravitational accelerations from the Sun and the Moon, all of which are conservative, as well as the aerodynamic drag and torque, the eddy-current torque, and the radiation pressure and torque, which are non-conservative. Direct solar radiation as well as reflected radiation (albedo) and infrared emission from the Earth are considered. The effect of hypervelocity impacts and internal energy dissipation are also taken into account. More complete forms than usually employed are used for: the gravity-gradient torque, calculated from a spherical harmonic representation of the Earth's gravitational potential; the aerodynamic drag and torque, for a spinning object; and the eddy-current torque, for a slowly rotating body.

Compared to the aforementioned spin models for geodetic satellites, D-SPOSE includes a few additional torques. In LOSSAM and LASSOS, the aerodynamic torque, internal dissipation, and hypervelocity impacts are not modeled as they are considered negligible. Furthermore, the magnetic torque definition we employ is more flexible and also applicable to asymmetrical satellites, not to mention contains higher-order terms of the magnetic potential. The most significant difference, however, is regarding the magnetic torque. In LOSSAM and LASSOS, the magnetic torque formulation is different from the eddy-current torque equation presented in this work; it is based on an integration of the complex polarizability per unit volume of the spherical satellite, which is a function of the penetration depth of the magnetic field in the body [18, 19]. However, such a formulation is not easily adaptable to defunct satellites with complex shapes, making the following formulation a necessity when discussing space debris.

Table 1: External perturbations considered in the coupled orbit-attitude propagation model

Perturbation	Environmental Model
Gravitational perturbations and gravity gradient torque	EGM2008 [24]
Third-body perturbations	Miriade Ephemerides [25]
Aerodynamic drag and torque	DTM-2013 [26]; NRLMSISE-00 [27]; JB-2008 [28]; HWM14 [29]
Eddy-current torque	IGRF-12 [30]; WMM [31]
Solar radiation pressure and torque	Montenbruck and Gill [32]
Albedo acceleration and torque	Stephens [33]; CERES [34]; ECMWF [35]
Infrared acceleration and torque	Stephens [33]; CERES [34]; ECMWF [35]
Internal energy dissipation	Kane Damper [36]
Hypervelocity impacts	Sagnières and Sharf [37, 38]; MASTER-2009 [39]

The equation previously used for the eddy-current torque is only valid for objects rotating quickly relative to their orbital rotation frequency [40, 41]. When the spin period of a spacecraft increases and becomes comparable to its orbital period, the time variation of the magnetic field as seen by the orbiting spacecraft needs to be considered. This improvement for slow-spinning spacecraft is also made in LASSOS compared to its predecessor LOSSAM, but for the different formulation. The new equation for the eddy-current torque becomes [7]:

$$\boldsymbol{\tau}_{\text{eddy}} = \left[\mathbf{M} \left(\boldsymbol{\omega} \times \mathbf{B} - \left(\frac{d\mathbf{B}}{dt} \right)_I \right) \right]^\times \mathbf{B} \quad (5)$$

where \mathbf{M} is the magnetic tensor of the object, \mathbf{B} is the Earth's magnetic field, and $\left(\frac{d\mathbf{B}}{dt} \right)_I$ is the time derivative of the Earth's magnetic field measured in the inertial frame as experienced along the satellite's orbit and expressed in the body-fixed frame. It can be calculated from the magnetic field in a rotating Earth-centered Earth-fixed (ECEF) frame:

$$\left(\frac{d\mathbf{B}}{dt} \right)_I = \left(\frac{d\mathbf{B}}{dt} \right)_E + \boldsymbol{\omega}_E \times \mathbf{B} \quad (6)$$

where $\boldsymbol{\omega}_E$ is the angular velocity of the Earth with respect to the inertial frame. Furthermore, the time derivative of the magnetic field measured in the ECEF frame can be expanded:

$$\left(\frac{d\mathbf{B}}{dt} \right)_E = (\mathbf{v}_E \cdot \nabla) \mathbf{B} + \left(\frac{\partial \mathbf{B}}{\partial t} \right)_E \quad (7)$$

where \mathbf{v}_E is the spacecraft velocity measured in the rotating ECEF frame:

$$\mathbf{v}_E = \mathbf{v} - \boldsymbol{\omega}_E \times \mathbf{r} \quad (8)$$

Considering a local spherical coordinate frame, S :

$$\left(\frac{\partial \mathbf{B}}{\partial t} \right)_E = \left(\frac{\partial \mathbf{B}}{\partial t} \right)_S + \boldsymbol{\omega}_S \times \mathbf{B} \quad (9)$$

where $\boldsymbol{\omega}_S$ is the angular velocity of the spherical coordinate frame with respect to the ECEF frame due to the

orbiting spacecraft, defined by:

$$\boldsymbol{\omega}_S = \frac{\mathbf{r} \times \mathbf{v}_E}{r^2} \quad (10)$$

Analytical expressions for these terms can be obtained from the spherical harmonic expression for the Earth's magnetic potential. In the current version of D-SPOSE, two geomagnetic models can be selected in order to obtain the value of the Earth's magnetic field: the International Geomagnetic Reference Field 12th edition (IGRF-12) or the World Magnetic Model (WMM) [30, 31]. The spherical harmonic expansion of the Earth's magnetic potential [20] can be written as:

$$\mathbf{B} = -\nabla V \quad (11)$$

$$V(r, \phi, \lambda) = a \sum_{n=1}^k \left(\frac{a}{r} \right)^{n+1} \sum_{m=0}^n (g_n^m \cos(m\lambda) + h_n^m \sin(m\lambda)) P_n^m[\cos \phi] \quad (12)$$

where ϕ is the colatitude, λ is the longitude, $a = 6371.2$ km is the geomagnetic convention for Earth's mean reference spherical radius, g and h are Gauss coefficients obtained from a magnetic potential model up to degree and order k , which is dependent on the chosen model, and P_n^m are the Schmidt normalized associated Legendre functions evaluated at $\cos \phi$. The analytical expressions derived for $\left(\frac{d\mathbf{B}}{dt} \right)_I$ from the spherical harmonic expansion of the Earth's magnetic field are detailed in Appendix A.

Another important addition to the previous model is the inclusion of the acceleration and torque due to Earth's albedo and infrared emissions. These two torques are not considered in LOSSAM and LASSOS. The acceleration associated with radiation can be calculated as a sum over every affected surface p [22]:

$$\mathbf{a}_{\text{rad}} = \sum_p \frac{\phi}{mc} \left[(\sigma_a + \sigma_{rd}) \mathbf{s} + \frac{2}{3} \sigma_{rd} \mathbf{n}_p + 2 \sigma_{rs} \cos \beta \mathbf{n}_p \right] A_p \cos \beta \quad (13)$$

where m is the spacecraft mass, σ_a , σ_{rd} , and σ_{rs} represent the coefficients of absorption, diffuse reflection, and specular reflection for that surface and for the appropriate spectrum, respectively, $c = 2.99792458 \times 10^8$ m s⁻¹

is the speed of light, ϕ is the radiation photon flux, \mathbf{s} is the unit vector of the incident light direction, and $\cos \beta = \mathbf{s} \cdot \mathbf{n}_p$, with \mathbf{n}_p the inward surface normal. Surfaces are considered to be in view of the radiation source when $\cos \beta > 0$.

The albedo and infrared radiation photon fluxes vary with time and location and need to be summed over every Earth surface element defined by latitude, θ , and longitude, λ , bins:

$$\phi_{\text{alb}} = S \left(\frac{a_u}{r_1} \right)^2 \sum_{\theta} \sum_{\lambda} \alpha_{\text{alb},\theta,\lambda} \cos \psi \cos \gamma \frac{A_{\theta,\lambda}}{\pi d} \quad (14)$$

$$\phi_{\text{ir}} = S \left(\frac{a_u}{r_1} \right)^2 \sum_{\theta} \sum_{\lambda} \alpha_{\text{ir},\theta,\lambda} \cos \gamma \frac{A_{\theta,\lambda}}{4\pi d} \quad (15)$$

where $S = 1361 \text{ W m}^{-2}$ is the solar radiation constant, $a_u = 1.495978707 \times 10^{11} \text{ m}$ is the astronomical unit, r_1 is the Earth-Sun distance, α_{alb} and α_{ir} are the albedo and emissivity coefficients, respectively, $A_{\theta,\lambda}$ is the Earth surface element area, d is the Earth surface element-satellite distance, and with ψ and γ representing the angles between the Earth surface element normal and the direction to the Sun and satellite, respectively. Earth surface elements are only considered when $\cos \gamma > 0$ for both albedo and infrared emissions, and also only when the surface element is lit, i.e. when $\cos \psi > 0$, for the albedo.

Three model choices for the Earth albedo and emissivity, each using $9^\circ \times 9^\circ$ latitude-longitude bins, are available in D-SPOSE. The first is a set of monthly-averaged values derived by Stephens [33] from satellite observations between 1964 and 1977. The second and third are obtained from two different observation centers: NASA's Clouds and the Earth's Radiant Energy System (CERES) and the European Centre for Medium-Range Weather Forecasts (ECMWF), both datasets obtained from monthly-averaged values from 2000-2015 satellite data [34, 35].

Although the contributions of the albedo and infrared radiation are expected to be minute for the geodetic satellites studied here, the effects of these perturbations will be much larger for box-wing satellites such as TOPEX/Poseidon, which is of considerable interest due to its spin up found to be due to radiation pressure [3]. Furthermore, the complete formulation of the eddy-current torque, as per Eq. 5, will have a large influence on the spin evolution of geodetic satellites as they experience an exponential decay of their angular velocity, leading them to rotational states where their orbital period is on the same order of magnitude as their spin period; this is currently the case for LAGEOS-2 [13].

A few other differences and improvements in the presented version of the propagator compared to our previous work have been incorporated [11]. Third-body perturbations are now calculated using the positions of the Sun and the Moon from available planetary ephemerides provided by the Virtual Observatory of the Institut

de Mécanique Céleste et de Calcul des Éphémérides (IMCCE) [25], interpolated linearly with 12-hour increments for the Sun, and 4-hour increments for the Moon, providing a more accurate orbital propagation necessary for precise attitude dynamics studies. Multiple thermospheric models are also available for the calculation of the atmospheric density at the satellite location. These include the Naval Research Laboratory Mass Spectrometer and Incoherent Scatter Extended 2000 model (NRLMSISE-00), the Jacchia-Bowman 2008 model (JB2008), and the Drag-Temperature Model 2013 (DTM-2013) [27, 28, 26]. There is also an option to assume horizontal winds due to a co-rotating atmosphere or to calculate deviations according to the Horizontal Wind Model 2014 (HWM14) [29].

2.2 D-SPOSE Inputs

One of the key aspects of the developed propagator is its flexibility. Five user-input files are expected to initialize the coupled propagation. First, a file containing a Two-Line Element (TLE) set in the standard format provides the information necessary to characterize the orbit and the initial epoch. This is preferred instead of using accurate position data from ILRS so as to have the possibility of use with objects which aren't necessarily tracked by laser ranging. Second is a file containing the propagation parameters, specifically information on the desired propagation time step, time length, and the frequency at which the user requires information on the state of the system throughout the propagation. The next file is one containing the model parameters: the user has the option to include or exclude every considered acceleration and torque, and to choose the desired environmental model for each. Furthermore, perturbation parameters such as the drag coefficient or damper properties for the internal dissipation are set up here as well.

The last two files are related to the spacecraft itself. The first contains information on the spacecraft geometry. Any spacecraft shape can easily be considered since the input consists of a list of triangular surfaces defined by the position of its three vertices in the body-fixed frame, the direction of its inward surface normal, and the optical coefficients in the visible and infrared spectra. The second file contains the other properties of the spacecraft: its mass, its moments of inertia and magnetic tensor in the same body-fixed frame, and for the calculation of hypervelocity impacts, the frequency of expected collisions and the proportion coming from micrometeoroids for the object's orbit. Finally, the initial orientation of the spacecraft either in the inertial frame or in the orbital frame at the initial epoch is requested.

Two output files are generated by the propagator: the first contains the evolution of the system state with information on the position (\mathbf{r}), velocity (\mathbf{v}), attitude

(\mathbf{q}), and angular velocity ($\boldsymbol{\omega}$) of the spacecraft; the second contains the values of the accelerations and torques considered throughout the propagation, as well as the total work done by the non-conservative perturbations on the spacecraft.

3 LAGEOS-2

As a result of the success of the LAGEOS mission launched in 1976, NASA and the Italian Space Agency (ASI) joined forces to build a twin satellite in order to continue the scientific endeavours of the original mission. LAGEOS-2 was finally launched on October 22, 1992 in a 52.6° inclined, nearly circular orbit at approximately 5,800 km altitude. Its mission objective was to provide laser ranging measurements for a variety of geodetic studies. As such, precise observations of the satellite's position have been made since its launch [13]. Furthermore, high repetition rate SLR data have made possible the determination of its spin period and spin axis orientation, which have enabled studies of general relativity effects such as the Lense-Thirring effect [42]. In addition, light curves coming off the spacecraft have been analyzed, providing another source of estimates of its spin period and spin axis orientation [16].

Much effort has already been made to try and understand the spin dynamics of the LAGEOS satellites [43, 18, 13, 19]. The goal of this study is not to try and improve these satellite-specific models, but to see whether the model we constructed for space debris remediation purposes could reproduce past observation results for LAGEOS-2. Simulations were therefore performed and compared to these observations.

Two major spacecraft parameters influence greatly the spacecraft spin dynamics due to the dominance of the torques associated with them: the moments of inertia, affecting the gravity-gradient torque, and the magnetic tensor, influencing the eddy-current torque. However, as it was not thought at the time of launch that such precise orbit measurements would be obtained or could be improved by measuring satellite's spin state, the spacecraft's moments of inertia were not determined before launch [44]. However, multiple efforts have been made to estimate them.

An in-depth review and critical analysis of past estimates of the mass and inertia properties of LAGEOS-2 were made as part of the LAsER RAnged Satellites Experiment (LARASE) research program [44]. This project aims to improve modelling and measurements of general relativity effects from satellite laser ranging data [42]. Conclusions on the LAGEOS-2 properties were drawn from all available information in the literature and from an analysis of the satellite's spin dynamics using the LOSSAM model; the estimated mass and moments of inertia of the satellite were $m = 405.38$ kg, $I_z = 11.45 \pm 0.03$ kg m² and $I_x = I_y = 11.00 \pm 0.03$ kg m²

[18, 44]. Furthermore, the satellite's center of mass was found to be -0.053 ± 0.025 cm from the geometric centre of the slightly oblate sphere along its symmetry axis, assumed here to be the z -axis, and the sphere's radius was estimated to be 30 cm [18]. Figure 1 shows the spacecraft geometry, divided into 264 surfaces, used as input into our propagator along with all of the parameters presented in Table 2.

The magnetic tensor, on the other hand, has never been estimated. In the case of LAGEOS-2, an initial estimate for the magnetic tensor can be obtained by considering the satellite as a thick spherical shell whose magnetic tensor in the body-fixed frame has previously been shown to be approximated by:

$$\mathbf{M} = \text{diag}\{M, M, M\} \quad (16)$$

with [45]:

$$M = \frac{2}{15} \pi \sigma \mu^2 (b^5 - a^5) \quad (17)$$

where σ is the body's electrical conductivity, μ is its relative permeability, and b and a are the shell's outer and inner radius, respectively.

Although the structure of the LAGEOS-2 spacecraft is complex, made up of elements composed of various materials, we can use the formulation in Eq. (17) to derive an estimate of the magnetic tensor. As LAGEOS-2 is coated with aluminum, whose conductivity is 2.459×10^7 S m⁻¹ and relative permeability approximated to 1, we can consider the spacecraft as an aluminum shell [18]. With a radius of 30 cm and a shell thickness of 1.5 cm, we obtain $M = 5662$ S m⁴; however, multiple simulations were executed by varying this value to obtain a best fit when comparing to observations.

The initial conditions of the satellite were selected from observations in early March 2000 and propagated for a period of 8 years with a time step of 1 s. A simulation with a time step of 0.1 s was also performed, showing no difference in the results, confirming internal conservation of energy. The following TLE was chosen to initialize the orbit:

```
1 22195U 92070B 00063.73989110 -0.00000009 00000-3 0 8627
2 22195 52.6411 214.8667 0137462 309.2891 49.5566 6.47294321174037
```

The initial spin period and orientation of the spin axis were taken from light curve observations at the same epoch: a spin period of 17.2712 s, the declination and right ascension (RA) of the spin axis of the satellite - 65.78° and 272.36° , respectively, assumed to be the z -axis [16]. All of the initial conditions are presented for LAGEOS-2 in Table 3 with the semi-major axis (a), the inclination (i), the eccentricity (e), the right ascension of the ascending node (Ω), and the argument of perigee (ω).

The optical coefficients for direct solar radiation were determined from previous studies [19]. A reflectivity coefficient of $C_r = 1.12$ with a reflectivity difference between the north and south hemispheres of the satellite

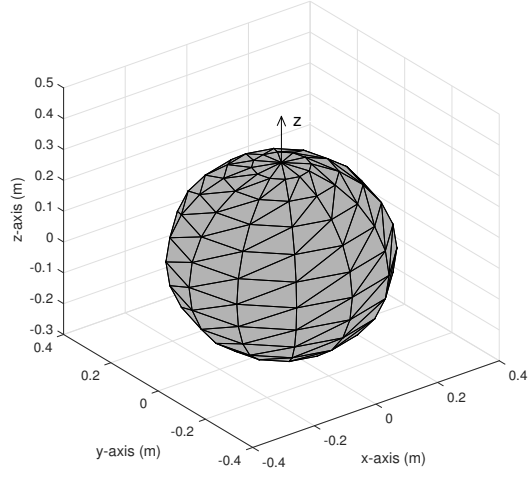


Figure 1: LAGEOS-2 Surface Geometry Model

Table 2: Spacecraft Parameters

Spacecraft	m (kg)	$I_x = I_y$ (kg m ²)	I_z (kg m ²)	r (cm)	h_{com} (cm)	C_r	ΔC_r	M (S m ⁴)
LAGEOS-2	405.38	11.00	11.45	30	-0.053	1.12	0.012	5900
LARES	386.8	4.76	4.77	18.2	0	1.07	0	450
Ajisai	685.1	485	525	107.5	0	1.12	0	625

Table 3: Initial Conditions

Spacecraft	Date	a (km)	i (°)	e	Ω (°)	ω (°)	Spin Period (s)	Declination (°)	RA (°)
LAGEOS-2	2000-03-03	12162	52.64	0.0137	214.87	309.29	17.2712	-65.78	272.36
LARES	2012-02-15	7820	69.49	0.0011	234.48	296.06	11.8	-73	186.5
Ajisai	2003-01-01	7867	50.01	0.0011	211.16	333.89	1.905	-87.5	-20

of $\Delta C_r = 0.012$ were found. From these, assuming that radiation is emitted diffusely, approximate values of σ_{rd} and σ_a of 0.17 and 0.83 for the north hemisphere, and 0.19 and 0.81 for the south hemisphere, respectively, were set.

In the simulations of LAGEOS-2, reflected and emitted radiation were not considered due to the negligible impact on a satellite of spherical shape. Aerodynamic drag and torque were also neglected due to the altitude of the satellite orbit. Hypervelocity impacts were neglected as well. Similarly, as the satellite is initially in a major-axis spin, internal energy dissipation was not considered.

Figure 2 shows the evolution of a) the spin period, b) the spin axis declination, and c) the spin axis right ascension in the inertial frame, for the entire propagation. The best fit simulation results obtained by varying the value of M only are presented with the black line, and observations made from SLR data are shown in blue [13], while the ones made from photometric measurements are shown in red [16]. A fit of the data is provided for the evolution of the inertial spin period [13]. The SLR data covers the period from 2000 to the end of 2007, while estimates obtained from light curves are available from 2000 to the end of 2004. As can be seen from the figure, using the input parameters stated in Table 2, simulations and observations agree well. The simulation shown was obtained with the value of $M = 5900 \text{ S m}^4$ used in the magnetic tensor, which is very close to the initial analytical estimate of 5662 S m^4 . An almost perfect agreement can be seen with light curve observations of the spin axis orientation, which show much less scatter than its SLR counterparts. The differences observed with SLR observations can most likely be attributed to uncertainty in the measurements, but could also come from uncertainty in input parameters. As was mentioned, the moments of inertia and other spacecraft parameters are not perfectly known and would have a noticeable impact on simulation results.

A more convenient way to visualize the motion of a spacecraft's spin axis is through a reference frame rotating with its precessing orbital plane. It has long been known that under the sole influence of the gravity-gradient torque, the motion of a spinning satellite's angular momentum vector forms a closed path in this frame [46, 47]. As the eddy-current torque slows down its rotation, however, the closed path will evolve. By defining the orbital plane with x_o pointing towards the ascending node and z_o pointing along the orbit normal, one can define in this frame two angles that characterize a satellite's angular momentum vector, or in our case its spin axis. Figure 3a defines the orbital frame in this way, with i and Ω representing the orbit inclination and right ascension of the ascending node, respectively. Figure 3b shows the two angles θ and ϕ defining the orientation of the spin axis in the orbital frame.

Making use of this reference frame which isolates the orbit's precession, Fig. 4 contains the evolution of both of these angles from the simulation throughout the entire propagation. Figure 4c characterizes the evolution of the spin axis in the orbital frame in an equidistant azimuthal projection along the line of sight of the orbit normal direction from the negative to the positive. The starting point of the motion on February 15, 2012 is indicated by a plus sign. As one can see, the LAGEOS-2 spin axis evolves towards a rotation about a point slightly displaced from the negative orbit normal with an increasing amplitude and decreasing period. This motion is similar to what was previously found for Envisat, whose angular momentum vector was determined to be experiencing a nutation about the negative orbit normal with an increasing amplitude along with a small libration [11].

4 LARES

On February 13, 2012, ESA launched the new Italian Laser Relativity Satellite (LARES) and placed it in a circular orbit at an altitude of 1450 km and an inclination of 69.5° . Its main mission was to send back observations of Earth's gravity field and provide much-needed geodetic measurements in combination with the LAGEOS program. Just like LAGEOS-2, it is a fully passive spherical satellite containing multiple CCRs on its surface for SLR observations.

First SLR measurements were obtained shortly after its launch, showing that although the body was made of a non-magnetic alloy so that the interaction with the Earth's magnetic field would be minimal, eddy-currents still occurred and slowed-down the satellite's spin [48]. A longer observation campaign, from February 2013 to April 2013, was then performed showing a precession of the spin axis; the LOSSAM model was applied to LARES and showed an agreement between simulation results and these observations [14].

Recently, the LASSOS model was developed to further the efforts of providing accurate modelling of the LAGEOS and LARES spin parameters [19], also providing accurate information on the input parameters for their model. Using these parameters, we tried to replicate the observations using D-SPOSE.

The surface geometry of LARES was assumed to be a sphere with a radius of 18.2 cm divided into 264 surfaces, similarly to LAGEOS-2 as shown in Fig. 1 but with the center of mass assumed to be at the sphere's geometric center, with moments of inertia values of $I_x = I_y = 4.76 \pm 0.03 \text{ kg m}^2$ and $I_z = 4.77 \pm 0.03 \text{ kg m}^2$ and a spacecraft weight of $m = 386.8 \text{ kg}$ [19]. The reflectivity coefficient was previously determined to be 1.07; so, under similar assumptions as for LAGEOS-2, the coefficients of absorption and diffuse reflection were set as 0.9 and 0.1, respectively, with no difference in reflectivity among both hemispheres [19]. The parameters that

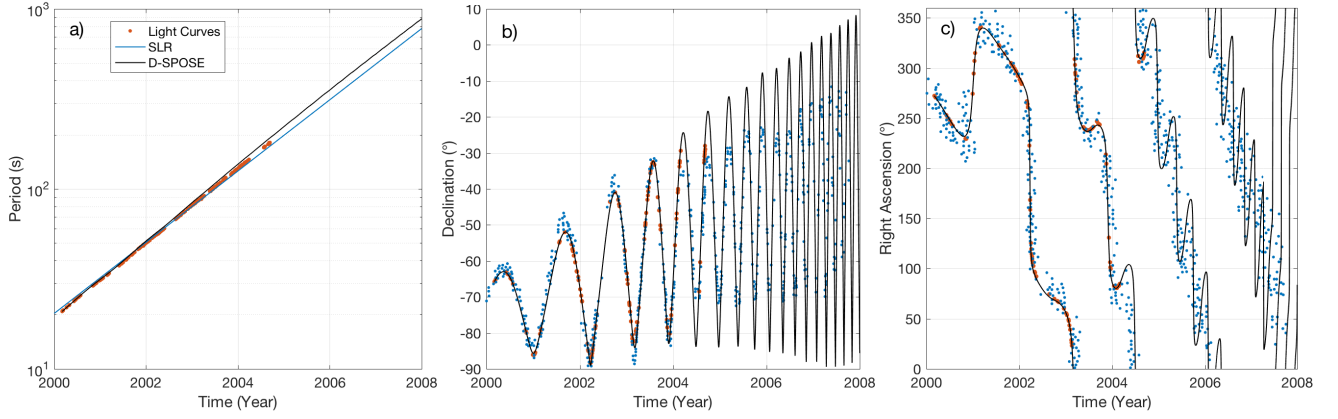


Figure 2: Evolution of LAGEOS-2 Spin Parameters in Inertial Frame

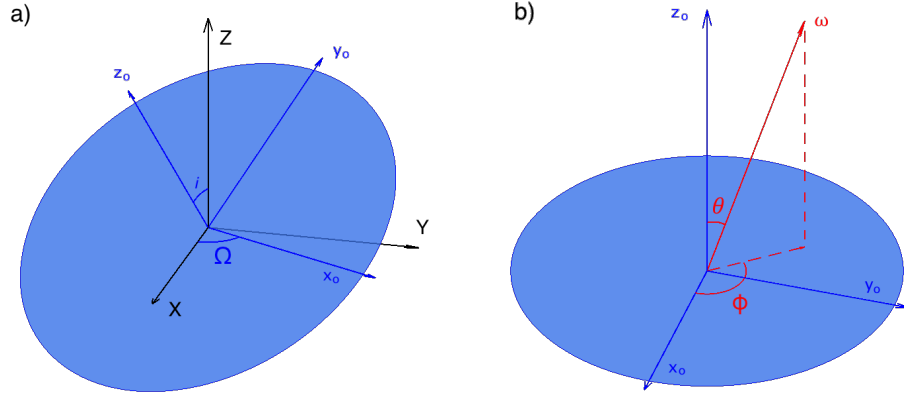


Figure 3: Orbital Reference Frame

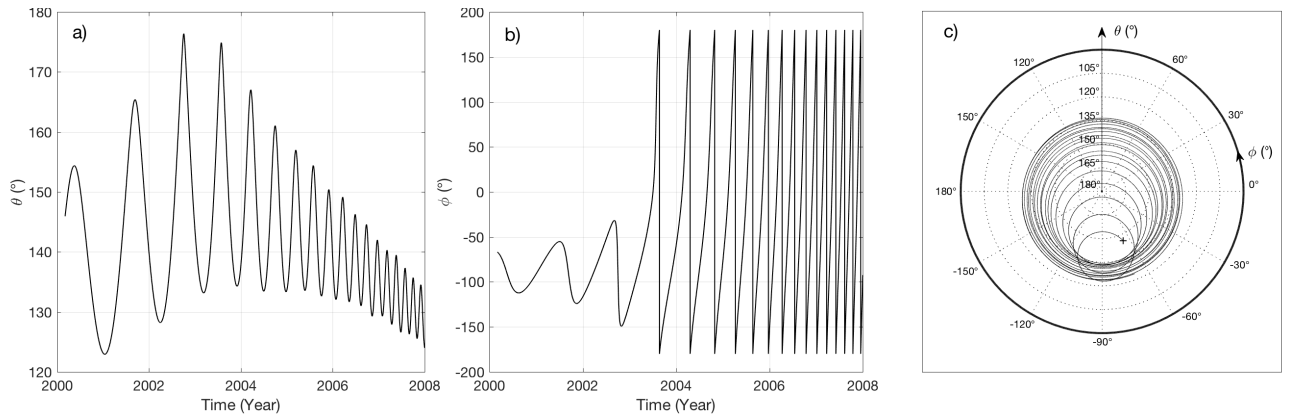


Figure 4: Evolution of LAGEOS-2 Spin Axis in Orbital Frame from Simulation

were used as input into the propagator for LARES are summarized in Table 2.

Again, aerodynamic perturbations, hypervelocity impacts, internal energy dissipation, and emitted and reflected radiation were not considered. The initial TLE was taken right after launch, in mid-February 2012, and the propagation length and time step were set to 1.5 years and 1 s, respectively:

```
1 38077U 12006A 12046.96446026 -.00000022 00000-0 10000-3 0 130
2 38077 69.4848 234.4843 0011091 296.0553 63.9332 12.54929120 333
```

The spin period and orientation of the spin axis were taken from SLR measurements right after launch: a spin period of 11.8 s, a spin axis orientation with a -73° declination and a 186.5° right ascension, assuming the spin axis of the satellite to be the z -axis [14]. These initial conditions, including the spin parameters and orbital elements at the TLE epoch are presented in Table 3. Figure 5 shows the evolution of a) the spin period, b) the spin axis declination, and c) the spin axis right ascension in the inertial frame for the entire propagation in black, with the SLR observations and a fit of the inertial spin period shown in blue [14].

Similarly to LAGEOS-2, an initial value for the magnetic tensor was obtained from Eq. (17). Assuming a similar structure to what was used for LAGEOS-2 but for an aluminum shell with a radius of 18.2 cm and a thickness of 1 cm, the initial value of $M = 506 \text{ S m}^4$ was set. In order to reproduce the spin period increase, however, a magnetic tensor of $M = 450 \text{ S m}^4$ was determined to provide the best fit, agreeing well with the initial estimate.

Once more, a good agreement exists between observations and simulation results. Nevertheless, a departure between both seems to appear towards the end of the propagation, again likely due to uncertainties in observations, but also in the input parameters used, particularly the moments of inertia, which play a crucial role in the precession motion of the spin axis under the influence of the gravity-gradient torque. More observations would be needed to investigate this further.

As was done for LAGEOS-2 in the previous section, the motion of the LARES spin axis in the orbital frame was analyzed. Figure 6 displays the evolution of the two angles θ and ϕ fixed with the precessing orbit for the 1.5-year propagation. Throughout the simulation, the spin axis seems to be rotating about a point approximately 110° from the orbit normal and -90° from the ascending node. The amplitude of the motion also seems to be decreasing with time, with one revolution completed in a little over six months. However, this represents only one and a half years and more observations would be needed to compare to simulations at a future date and to fully characterize the resulting motion.

5 Ajisai

Originally named the Experimental Geodetic Payload, Ajisai is a Japanese satellite that was launched in August 1986 in an orbit of 1500 km and 50° inclination. It is a passive geodetic satellite that had the purpose of improving Japan's geodetic network and calculating the accurate positions of the many Japanese islands. It contains 1436 CCRs as well as a nutation damper, limiting the effect of external perturbations helping to maintain a major-axis spin [49]. However, being much larger than the two previous satellites with a radius of 107.5 cm but in the same mass range ($m = 685.1$), its high area-to-mass ratio leads to higher uncertainty from non-gravitational perturbations [49]. The spacecraft was originally launched in a spinning state with a spin period of 1.5 s and with its spin axis aligned with the Earth's rotation axis.

Like LAGEOS-2 and LARES, it has been continuously tracked by satellite laser ranging stations and photometric measurements have been made throughout its lifetime. The high repetition rate SLR station in Graz, Austria has provided observations from thousands of satellite passes. An analysis of 4599 passes from October 2003 to November 2014 from which the spin axis orientation was obtained revealed a precession and nutation of the Ajisai spin axis, similar to what was seen for the two satellites in the previous sections [15]. Moreover, 279 photometric observations have been analyzed from 2009 to the end of 2015 [17] providing additional measurements of the satellite's spin axis orientation and spin period. These two datasets are shown in Fig. 7 and represent the largest observation data set among the three spacecraft considered.

In order to validate our propagator, a simulation was run for Ajisai and compared to these observations. The satellite mass and radius were set to be 685.1 kg and 1.075 m [49]. The surface geometry was divided into 264 surfaces. The same reflectivity coefficient as LAGEOS-2 was used, with no difference between the hemispheres and no offset of the center of mass with the geometric center as no accurate data was available.

Similarly to LAGEOS-2 and LARES, little information exists in the literature on Ajisai's inertia properties. During the analysis of the SLR measurements, an estimate of $I_z = 527.7 \text{ kg m}^2$ and a ratio of the principal moments of inertia of 1.09 was determined [50, 15]. Approximate values of $I_x = I_y = 485 \text{ kg m}^2$ and $I_z = 525 \text{ kg m}^2$ were therefore used in our simulations.

The estimation of the magnetic tensor is more complicated for Ajisai than it was for the other two spacecraft. The composition of Ajisai is very different from LAGEOS-2 and LARES; Ajisai was built to minimize the effect of eddy currents, with dielectric film placed in layers in the body's external structure [15]. Eddy-currents therefore have a much smaller influence than they do for

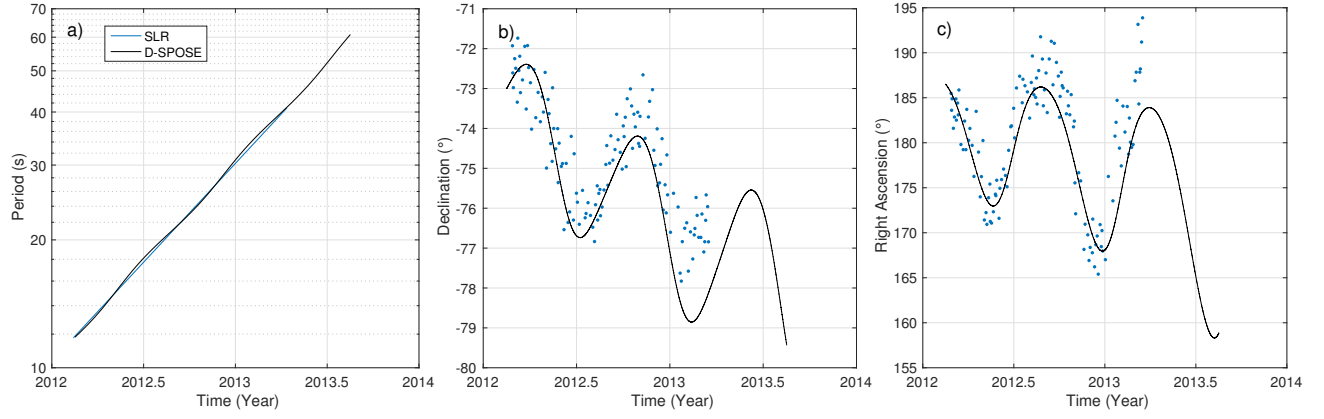


Figure 5: Evolution of LARES Spin Parameters in Inertial Frame

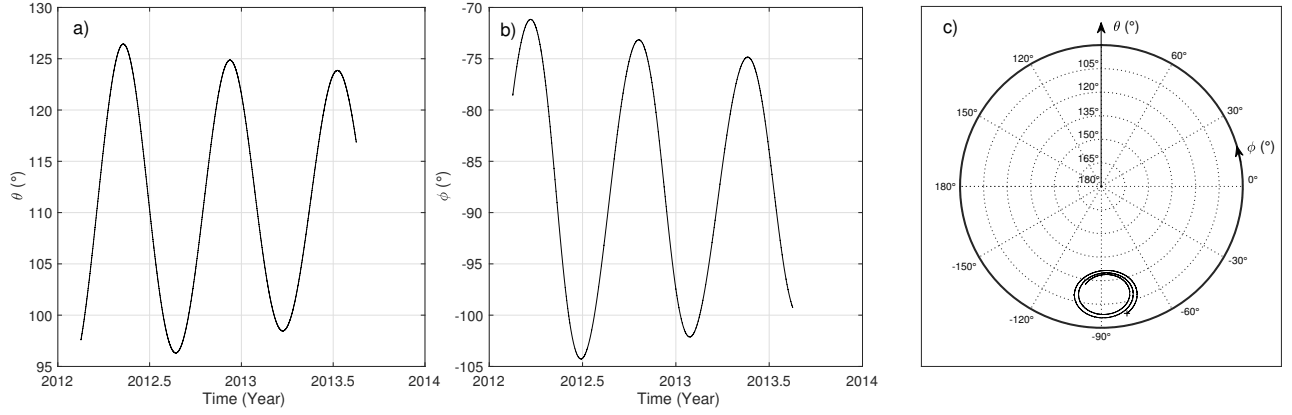


Figure 6: Evolution of LARES Spin Axis in Orbital Frame from Simulation

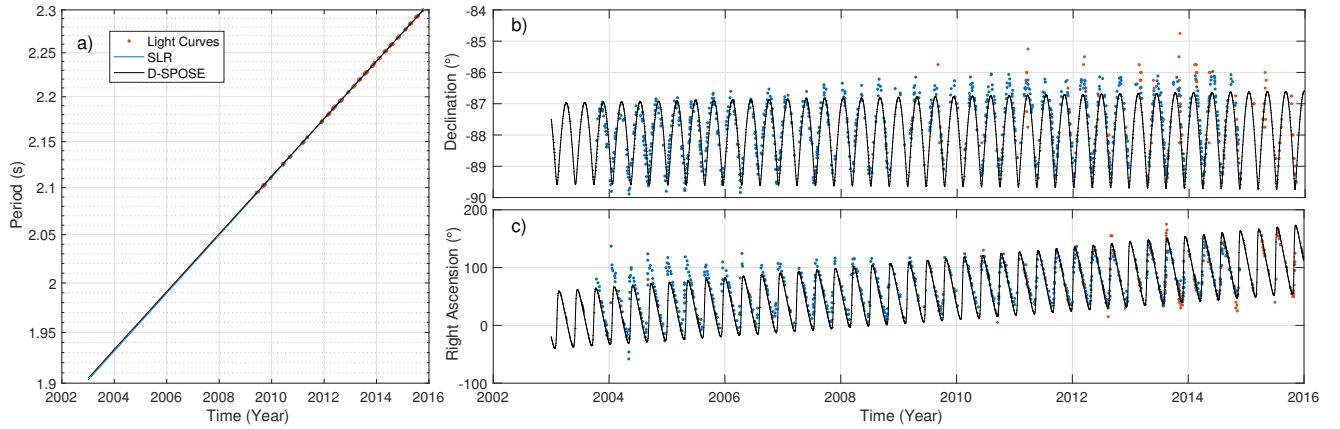


Figure 7: Evolution of Ajisai Spin Parameters in Inertial Frame

the other spacecraft, a fact that is observable in the slow increase of its spin period over the 13-year observation time frame shown in Fig. 7. Nevertheless, the best fit for the magnetic tensor was found to be 625 S m^4 . The parameters that were used as input into the propagator for Ajisai are summarized in Table 2.

The spin period and orientation of the spin axis were estimated for early 2003: a spin period of 1.905 s, and a spin axis orientation with a -87.5° declination and a -20° right ascension were used for initial conditions, again assuming the spin axis of the satellite to be the z -axis. The initial TLE was taken at the beginning of 2003, at the start of the SLR observations:

```
1 16908U 86061A 03001.47495629 -.00000083 00000-0 10000-3 0 7483
2 16908 50.0093 211.1607 0011280 333.8863 26.1414 12.44446750413909
```

The initial conditions for Ajisai, including the spin parameters and orbital elements at the TLE epoch are presented in Table 3. The results of the propagation are presented in Fig. 7, with a) the spin period, b) the spin axis declination, and c) the spin axis right ascension in the inertial frame for the entire propagation in black. The SLR and light curve observations are shown in blue and red, respectively [15, 17]. Aerodynamic perturbations, hypervelocity impacts, internal energy dissipation, and emitted and reflected radiation were not considered in the simulations. A propagation length of 13 years was selected to cover the observation time span. A time step of 0.5 s was chosen as Ajisai is spinning very quickly compared to the other two spacecraft and the usual time step of 1 s was adequate to conserve energy; a subsequent check with a time step of 0.1 s did not show any differences compared to the results obtained with a time step of 0.5 s.

Once more, the results agree well with the observations, taking into account the uncertainty related to both datasets. Both sources of observations, SLR and light curves, show a similar scatter of observations and a similar agreement with the simulation results. The spin period increase is well captured using the determined magnetic tensor value of 625 S m^4 . There is, however, a small discrepancy seen in the right ascension at the beginning of the propagation. Nevertheless, if we take into account the fact that the declination is very close to -90° , for large fluctuations of the right ascension, the actual angular difference in the spin axis orientation at that declination is very small.

Switching over to the orbital frame, Fig. 8 shows the evolution of the two angles θ and ϕ fixed with the precessing orbit for the 13-year propagation. As we can see, the spin axis is very much fixed in this reference frame at a point close to 131° from the orbit normal and -90° from the ascending node. A small increase in the amplitude of the oscillation can be seen, showing the increasing effect of the external perturbations as the spacecraft steadily slows down.

6 Conclusion

Studying the spin dynamics of defunct spacecraft is of the utmost importance when considering their retrieval from orbit. The novel propagator developed for such studies, called D-SPOSE, was presented and validated by comparing simulation results to observations from three passive spherical geodetic satellites, LAGEOS-2, LARES, and Ajisai, for which observations of their spin state were abundant. The underlying model was described, building on the work presented in [11]. Although previous spin models existed for these satellites, D-SPOSE is to be more generic, flexible, and applicable to any type of passive or defunct spacecraft, where other external perturbations could also be prominent. The tool will be publicly available by the end of 2018 on the McGill Aerospace Mechatronics Laboratory GitHub: <https://github.com/McGill-AML>.

Even though it is coded in C for efficiency, the tool is very computationally demanding as a small time step for accurate attitude evolution, on the order of seconds or less, is needed compared to a propagation length on the time scale of years. Future improvements to the model could be made in order to be applied to certain types of satellites. Such improvements could include adding external perturbations like thermal forces and the YORP effect, usually important for box-wing satellites at very high altitudes.

High-repetition rate satellite laser ranging observations and light curve measurements from the three spacecraft were shown to agree very well with results from the propagator, confirming its use and benefit for future analyses of the rotational dynamics of large space debris. Some discrepancies exist, especially when comparing simulations to SLR observations, but these are due to the fact that relatively large uncertainties in observations are present and that the inertia and magnetic properties of the spacecraft are not well known. Furthermore, it was shown that studying the spin dynamics of satellites orbiting Earth is more convenient when looked at from the perspective of the rotating reference frame precessing with the orbit. This is due to the fact that, when dominant, the gravity-gradient torque forces a closed-loop motion of a satellite's spin axis in this frame.

Acknowledgments

The authors would like to thank Toshimichi Otsubo and Nikolay Koshkin for providing their observations of Ajisai and LAGEOS-2, respectively. This work was supported by Hydro-Québec and the Faculty of Engineering at McGill University through the McGill Engineering Doctoral Award. The authors are further grateful for the support of the Institut de Mécanique Céleste et de Calcul des Éphémérides (IMCCE), Natural Sciences and Engineering Research Council of Canada (NSERC),

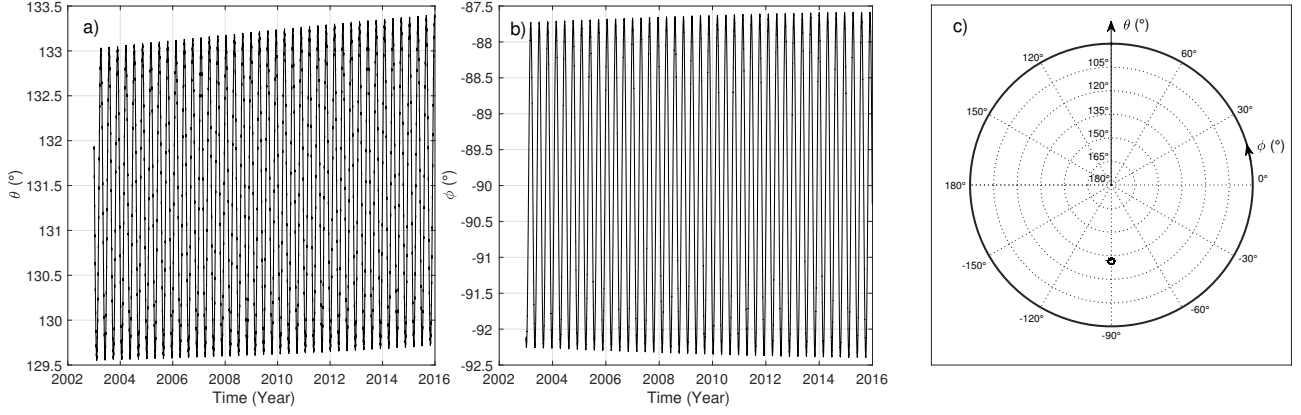


Figure 8: Evolution of Ajisai Spin Axis in Orbital Frame from Simulation

the Fonds de recherche du Québec - Nature et technologies (FRQNT) and Mitacs. Computations were made on the supercomputer Guillimin from McGill University, managed by Calcul Québec and Compute Canada. The operation of this supercomputer is funded by the Canada Foundation for Innovation (CFI), ministère de l'Économie, de la Science et de l'Innovation du Québec (MESI) and the FRQNT.

Appendix A

The following will go through the analytical expressions of the terms in the equation for the eddy-current torque as a function of the spherical harmonic expansion of the Earth's magnetic field. In the local spherical coordinate reference frame, defined by $\hat{\mathbf{r}}$ in the radial direction, $\hat{\boldsymbol{\phi}}$ in the south direction, and $\hat{\boldsymbol{\lambda}}$ in the east direction, the following can be written as:

$$\mathbf{B} = \begin{bmatrix} B_r \\ B_\phi \\ B_\lambda \end{bmatrix} = - \begin{bmatrix} \frac{\partial V}{\partial r} \\ \frac{1}{r} \frac{\partial V}{\partial \phi} \\ \frac{1}{r \sin \phi} \frac{\partial V}{\partial \lambda} \end{bmatrix} \quad (18)$$

$$\left(\frac{\partial \mathbf{B}}{\partial t} \right)_S = \begin{bmatrix} \frac{\partial B_r}{\partial t} \\ \frac{\partial B_\phi}{\partial t} \\ \frac{\partial B_\lambda}{\partial t} \end{bmatrix} = - \begin{bmatrix} \frac{\partial^2 V}{\partial r \partial t} \\ \frac{1}{r} \frac{\partial^2 V}{\partial \phi \partial t} \\ \frac{1}{r \sin \phi} \frac{\partial^2 V}{\partial \lambda \partial t} \end{bmatrix} \quad (19)$$

$$\begin{aligned} (\mathbf{v}_E \cdot \nabla) \mathbf{B} &= v_r \frac{\partial \mathbf{B}}{\partial r} + \frac{v_\phi}{r} \frac{\partial \mathbf{B}}{\partial \phi} + \frac{v_\lambda}{r \sin \phi} \frac{\partial \mathbf{B}}{\partial \lambda} \\ &= - \begin{bmatrix} v_r \frac{\partial^2 V}{\partial r^2} + \frac{v_\phi}{r} \frac{\partial^2 V}{\partial \phi \partial r} + \frac{v_\lambda}{r \sin \phi} \frac{\partial^2 V}{\partial \lambda \partial r} \\ \frac{v_r}{r} \frac{\partial^2 V}{\partial \phi \partial r} - \frac{v_r}{r^2} \frac{\partial V}{\partial \phi} + \frac{v_\phi}{r^2} \frac{\partial^2 V}{\partial \phi^2} + \frac{v_\lambda}{r^2 \sin \phi} \frac{\partial^2 V}{\partial \phi \partial \lambda} \\ \frac{v_r}{r \sin \phi} \frac{\partial^2 V}{\partial \lambda \partial r} - \frac{v_r}{r^2 \sin \phi} \frac{\partial V}{\partial \lambda} - \frac{v_\phi \cos \phi}{r^2 \sin^2 \phi} \frac{\partial V}{\partial \lambda} + \frac{v_\phi}{r^2 \sin^2 \phi} \frac{\partial^2 V}{\partial \lambda \partial \phi} + \frac{v_\lambda}{r^2 \sin^2 \phi} \frac{\partial^2 V}{\partial \lambda^2} \end{bmatrix} \end{aligned} \quad (20)$$

The partial derivatives of the magnetic potential can be calculated as follows:

$$\frac{\partial V}{\partial r} = - \sum_{n=1}^k \left(\frac{a}{r} \right)^{n+2} (n+1) \sum_{m=0}^n (g_n^m \cos(m\lambda) + h_n^m \sin(m\lambda)) P_n^m[\cos \phi] \quad (21)$$

$$\frac{\partial V}{\partial \phi} = a \sum_{n=1}^k \left(\frac{a}{r} \right)^{n+1} \sum_{m=0}^n (g_n^m \cos(m\lambda) + h_n^m \sin(m\lambda)) \frac{\partial P_n^m[\cos \phi]}{\partial \phi} \quad (22)$$

$$\frac{\partial V}{\partial \lambda} = a \sum_{n=1}^k \left(\frac{a}{r} \right)^{n+1} \sum_{m=0}^n m (-g_n^m \sin(m\lambda) + h_n^m \cos(m\lambda)) P_n^m[\cos \phi] \quad (23)$$

Similarly, the second partial derivatives of the magnetic potential can be calculated as follows:

$$\frac{\partial^2 V}{\partial r^2} = \frac{1}{r} \sum_{n=1}^k \left(\frac{a}{r} \right)^{n+2} (n+1)(n+2) \sum_{m=0}^n (g_n^m \cos(m\lambda) + h_n^m \sin(m\lambda)) P_n^m[\cos \phi] \quad (24)$$

$$\frac{\partial^2 V}{\partial \phi \partial r} = - \sum_{n=1}^k \left(\frac{a}{r} \right)^{n+2} (n+1) \sum_{m=0}^n (g_n^m \cos(m\lambda) + h_n^m \sin(m\lambda)) \frac{\partial P_n^m[\cos \phi]}{\partial \phi} \quad (25)$$

$$\frac{\partial^2 V}{\partial \lambda \partial r} = \sum_{n=1}^k \left(\frac{a}{r} \right)^{n+2} (n+1) \sum_{m=0}^n m (g_n^m \sin(m\lambda) - h_n^m \cos(m\lambda)) P_n^m[\cos \phi] \quad (26)$$

$$\frac{\partial^2 V}{\partial t \partial r} = - \sum_{n=1}^k \left(\frac{a}{r} \right)^{n+2} (n+1) \sum_{m=0}^n (\dot{g}_n^m \cos(m\lambda) + \dot{h}_n^m \sin(m\lambda)) P_n^m[\cos \phi] \quad (27)$$

$$\frac{\partial^2 V}{\partial \phi^2} = a \sum_{n=1}^k \left(\frac{a}{r}\right)^{n+1} \sum_{m=0}^n (g_n^m \cos(m\lambda)) \quad (42)$$

$$+ h_n^m \sin(m\lambda) \frac{\partial^2 P_n^m[\cos \theta]}{\partial \theta^2}$$

$$\frac{\partial^2 V}{\partial \lambda \partial \phi} = a \sum_{n=1}^k \left(\frac{a}{r}\right)^{n+1} \sum_{m=0}^n m(-g_n^m \sin(m\lambda))$$

$$+ h_n^m \cos(m\lambda) \frac{\partial P_n^m[\cos \theta]}{\partial \theta}$$

$$\frac{\partial^2 V}{\partial t \partial \phi} = a \sum_{n=1}^k \left(\frac{a}{r}\right)^{n+1} \sum_{m=0}^n (\dot{g}_n^m \cos(m\lambda))$$

$$+ \dot{h}_n^m \sin(m\lambda) \frac{\partial P_n^m[\cos \theta]}{\partial \theta}$$

$$\frac{\partial^2 V}{\partial \lambda^2} = -a \sum_{n=1}^k \left(\frac{a}{r}\right)^{n+1} \sum_{m=0}^n m^2 (g_n^m \cos(m\lambda))$$

$$+ h_n^m \sin(m\lambda) P_n^m[\cos \theta]$$

$$\frac{\partial^2 V}{\partial t \partial \lambda} = a \sum_{n=1}^k \left(\frac{a}{r}\right)^{n+1} \sum_{m=0}^n m(-\dot{g}_n^m \sin(m\lambda))$$

$$+ \dot{h}_n^m \cos(m\lambda) P_n^m[\cos \theta]$$

The Schmidt normalized associated Legendre functions, P_n^m , are related to the Gauss functions, $P^{n,m}$, by the following:

$$P_n^m = S_{n,m} P^{n,m} \quad (33)$$

using the transformations obtained by recursion:

$$S_{0,0} = 1$$

$$S_{n,0} = S_{n-1,0} \frac{2n-1}{n} \quad (34)$$

$$S_{n,n} = S_{n,m-1} \sqrt{\frac{(n-m+1)(\delta_m^1 + 1)}{n+m}}$$

The Gauss functions and its derivatives can also be obtained by recursion:

$$P^{0,0} = 1 \quad (35)$$

$$P^{1,0} = \cos \theta \quad (36)$$

$$P^{n,n} = \sin \theta P^{n-1,n-1} \quad (37)$$

$$P^{n,m} = \cos \theta P^{n-1,m} - K^{n,m} P^{n-2,m} \quad (38)$$

$$\frac{\partial P^{0,0}}{\partial \theta} = 0 \quad (39)$$

$$\frac{\partial P^{1,0}}{\partial \theta} = -\sin \theta \quad (40)$$

$$\frac{\partial P^{n,n}}{\partial \theta} = \sin \theta \frac{\partial P^{n-1,n-1}}{\partial \theta} + \cos \theta P^{n-1,n-1} \quad (41)$$

$$\frac{\partial P^{n,m}}{\partial \theta} = \cos \theta \frac{\partial P^{n-1,m}}{\partial \theta} - \sin \theta P^{n-1,m} - K^{n,m} \frac{\partial P^{n-2,m}}{\partial \theta}$$

$$(28) \quad \frac{\partial^2 P^{0,0}}{\partial \phi^2} = 0 \quad (43)$$

$$\frac{\partial^2 P^{1,0}}{\partial \phi^2} = -\cos \phi \quad (44)$$

$$(29) \quad \frac{\partial^2 P^{n,n}}{\partial \phi^2} = 2 \cos \phi \frac{\partial P^{n-1,n-1}}{\partial \phi} - \sin \phi P^{n-1,n-1}$$

$$+ \sin \phi \frac{\partial^2 P^{n-1,n-1}}{\partial \phi^2} \quad (45)$$

$$(30) \quad \frac{\partial^2 P^{n,m}}{\partial \phi^2} = \cos \phi \frac{\partial^2 P^{n-1,m}}{\partial \phi^2} - 2 \sin \phi \frac{\partial P^{n-1,m}}{\partial \theta}$$

$$- \cos \phi P^{n-1,m} - K^{n,m} \frac{\partial^2 P^{n-2,m}}{\partial \phi^2} \quad (46)$$

with, for $n = 1$:

$$K^{n,m} = 0 \quad (47)$$

and, for $n \geq 2$:

$$K^{n,m} = \frac{(n-1)^2 - m^2}{(2n-1)(2n-3)} \quad (48)$$

References

- [1] Liou, J.-C., and N. L. Johnson (2006), Risks in Space from Orbiting Debris, Science, 311, 340-341, doi:10.1126/science.1121337.
- [2] Shan, M., J. Guo, and E. Gill (2016), Review and comparison of active space debris capturing and removal methods, Progress in Aerospace Sciences, 80(C), 18-32, doi:10.1016/j.paerosci.2015.11.001.
- [3] Kucharski, D. et al. (2017), Photon Pressure Force on Space Debris TOPEX/Poseidon Measured by Satellite Laser Ranging, Earth and Space Science, 4(10), 661-668, doi:10.1016/j.asr.2015.02.018.
- [4] Koshkin, N., E. Korobeynikova, L. Shakun, S. Strakhova, and Z. H. Tang (2016), Remote Sensing of the EnviSat and Cbers-2B satellites rotation around the centre of mass by photometry, Advances in Space Research, 58(3), 358-371, doi:10.1016/j.asr.2016.04.024.
- [5] Kucharski, D. et al. (2014), Attitude and Spin Period of Space Debris Envisat Measured by Satellite Laser Ranging, IEEE Transactions on Geoscience and Remote Sensing, 52(12), 7651-7657, doi:10.1109/TGRS.2014.2316138.
- [6] Earl, M. A., and G. A. Wade (2015), Observations of the Spin-Period Variations of Inactive Box-Wing Geosynchronous Satellites, Journal of Spacecraft and Rockets, 52(3), 968-977, doi:10.2514/1.A33077.

- [7] Efimov, S., Pritykin, D., and Sidorenko, V. (2018), Defunct Satellites in Nearly Polar Orbits: Long-term Evolution of Attitude Motion, *Open Astronomy*, submitted.
- [8] Efimov, S., Pritykin, D., and Sidorenko, V. (2018), Long-term Attitude Dynamics of Space Debris in Sun-synchronous Orbits: Cassini Cycles and Chaotic Stabilization, *Celestial Mechanics and Dynamical Astronomy*, submitted.
- [9] Kanzler, R., J. Silha, T. Schildknecht, B. Fritsche, T. Lips, and H. Krag (2015), Space debris attitude simulation - ι OTA (In-Orbit Tumbling Analysis), *Proceedings of the 2015 Advanced Maui Optical and Space Surveillance Technologies Conference*, 15-18 September, Maui, Hawaii.
- [10] Albuja, A. A., D. J. Scheeres, R. L. Cognion, W. Ryan, and E. V. Ryan (2018), The YORP effect on the GOES 8 and GOES 10 satellites: A case study, *Advances in Space Research*, 61, 122-144, doi:10.1016/j.asr.2017.10.002.
- [11] Sagnières, L. B. M., and Sharf, I. (2018), Long-term rotational motion analysis and comparison to observations of the inoperative Envisat, *Journal of Guidance, Control, and Dynamics*, 2018, accepted.
- [12] Pearlman, M. R., Degnan, J. J., and Bosworth, J. M. (2002), The International Laser Ranging Service, *Advances in Space Research*, 30(2), 135-143.
- [13] Kucharski, D., H. C. Lim, G. Kirchner, and J. Y. Hwang (2013), Spin parameters of LAGEOS-1 and LAGEOS-2 spectrally determined from Satellite Laser Ranging data, *Advances in Space Research*, 52(7), 1332-1338, doi:10.1016/j.asr.2013.07.007.
- [14] Kucharski, D., Hyung-Chul Lim, G. Kirchner, T. Otsubo, G. Bianco, and Joo-Yeon Hwang (2014), Spin Axis Precession of LARES Measured by Satellite Laser Ranging, *IEEE Geosci. Remote Sensing Lett.*, 11(3), 646-650, doi:10.1109/LGRS.2013.2273561.
- [15] Kucharski, D., G. Kirchner, T. Otsubo, H.-C. Lim, J. Bennett, F. Koidl, Y.-R. Kim, and J.-Y. Hwang (2016), Confirmation of gravitationally induced attitude drift of spinning satellite Ajisai with Graz high repetition rate SLR data, *Advances in Space Research*, 57(4), 983-990, doi:10.1016/j.asr.2015.12.010.
- [16] Otsubo, T., R. A. Sherwood, P. Gibbs, and R. Wood (2004), Spin Motion and Orientation of LAGEOS-2 From Photometric Observation, *IEEE Transactions on Geoscience and Remote Sensing*, 42(1), 202-208, doi:10.1109/TGRS.2003.817191.
- [17] Koshkin, N., L. Shakun, N. Burlak, E. Korobeynikova, S. Strakhova, S. Melikyants, S. Terpan, and A. Ryabov (2017), Ajisai spin-axis precession and rotation-period variations from photometric observations, *Advances in Space Research*, 60(7), 1389-1399, doi:10.1016/j.asr.2017.06.045.
- [18] Andrés de la Fuente, J. I. (2007), Enhanced Modelling of LAGEOS Non-Gravitational Perturbations, PhD Thesis, Technische Universiteit Delft.
- [19] Visco, M., and D. M. Lucchesi (2018), Comprehensive model for the spin evolution of the LAGEOS and LARES satellites, *Physical Review D*, 98(4), 044034, doi:10.1103/PhysRevD.98.044034.
- [20] Vallado, D. (2013), *Fundamentals of Astrodynamics and Applications*, Fourth Edition, Microcosm Press, Hawthorne, California. ISBN: 978-1881883180.
- [21] Vallado, D. A., Crawford, P., Hujsak, R., and Kelso, T. S. (2006), Revisiting Spacetrack Report #3: Rev 2, *Proceedings of the 2006 AIAA/AAS Astrodynamics Specialist Conference and Exhibit*, AIAA 2006-6753-Rev2, 21-24 August, Keystone, Colorado.
- [22] Hughes, P. C. (2006), *Spacecraft Attitude Dynamics*, Dover Publications, Inc., Mineola, New York. ISBN: 978-0-486-43925-9.
- [23] Dormand, J. R., and Prince, P. J. (1980), A family of embedded Runge-Kutta formulae, *Journal of Computational and Applied Mathematics*, 6(1), 19-26. doi:10.1016/0771-050X(80)90013-3.
- [24] Pavlis, N. K., Holmes, S. A., Kenyon, S. C., and Factor, J. K. (2012), The development and evaluation of the Earth Gravitational Model 2008 (EGM2008), *Journal of Geophysical Research*, 117, B04406, doi:10.1029/2011JB008916.
- [25] Institut de Mécanique Céleste et de Calcul des Ephémérides (2018), *Miriade - The Virtual Observatory Solar System Object Ephemeris Generator*, <<http://vo.imcce.fr/webservices/miriade/>>, accessed 2018-08-01.
- [26] Bruinsma, S.L. (2015), The DTM-2013 thermosphere model, *Journal of Space Weather and Space Climate*, 5, A1, doi:10.1051/swsc/2015001.
- [27] Picone, J. M., A. E. Hedin, D. P. Drob, and A. C. Aikin (2002), NRLMSISE-00 empirical model of the atmosphere: Statistical comparisons and scientific issues, *Journal of Geophysical Research*, 107(A12), 1468, doi:10.1029/2002JA009430.
- [28] Bowman, B. R. (2008), A New Empirical Thermospheric Density Model JB2008 Using New Solar and Geomagnetic Indices, *Proceedings of the 2008 AIAA/AAS Astrodynamics Specialist Conference and Exhibit*, AIAA 2008-6438, Honolulu, Hawaii, doi:10.2514/6.2008-6438.

- [29] Drob, D.P., et al. (2015), An update to the Horizontal Wind Model (HWM): The quiet time thermosphere, *Earth and Space Science*, 2, 301-3019, doi:10.1002/2014EA000089.
- [30] Thébaud, E., et al. (2015), International Geomagnetic Reference Field: the 12th generation, *Earth, Planets and Space*, 67, 79, doi:10.1186/BF03352355.
- [31] Chulliat, A., S. Macmillan, P. Alken, C. Beggan, M. Nair, B. Hamilton, A. Woods, V. Ridley, S. Maus, and A. Thomson (2015), The US/UK World Magnetic Model for 2015-2020, National Geophysical Data Center, NOAA.
- [32] Montenbruck, O., and Gill, E. (2012), *Satellite Orbits: Models, Methods, Applications*, Springer-Verlag Berlin Heidelberg. ISBN: 978-3-540-67280-7.
- [33] Stephens, G. L., G. G. Campbell, and T. H. Vonder Haar (1981), Earth Radiation Budgets, *Journal of Geophysical Research*, 86, 9739-9760.
- [34] Loeb, N. G., B. A. Wielicki, D. R. Doelling, G. L. Smith, D. F. Keyes, S. Kato, N. Manalo-Smith, and T. Wong (2009), Toward Optimal Closure of the Earth's Top-of-Atmosphere Radiation Budget, *J. Climate*, 22(3), 748-766, doi:10.1175/2008JCLI2637.1.
- [35] European Centre for Medium-Range Weather Forecasts (2018), Public Datasets, <<http://apps.ecmwf.int/datasets/>>, accessed 2018-08-01.
- [36] Kane, T. R., and Barba, P. M. (1966), Effects of Energy Dissipation on a Spinning Satellite, *AIAA Journal*, 4, 1391-1394, doi:10.2514/3.3683.
- [37] Sagnières, L. B. M., and Sharf, I. (2017), Stochastic modeling of hypervelocity impacts in attitude propagation of space debris, *Advances in Space Research*, 59, 1128-1143, doi:10.1016/j.asr.2016.11.030.
- [38] Sagnières, L. B. M., and Sharf, I. (2017), Evolution of spacecraft orbital motion due to hypervelocity impacts with debris and meteoroids, *Proceedings of the 7th European Conference on Space Debris*, 17-21 April, Darmstadt, Germany.
- [39] Flegel, S., et al. (2011), Maintenance of the ESA MASTER Model - Final Report, European Space Agency, Technical Report 21705/08/D/HK.
- [40] Praly, N., M. Hillion, C. Bonnal, J. Laurent-Varin, and N. Petit (2012), Study on the eddy current damping of the spin dynamics of space debris from the Ariane launcher upper stages, *Acta Astronautica*, 76(C), 145-153, doi:10.1016/j.actaastro.2012.03.004.
- [41] Ortiz Gómez, N., and S. J. I. Walker (2015), Eddy currents applied to de-tumbling of space debris: Analysis and validation of approximate proposed methods, *Acta Astronautica*, 114(C), 34-53, doi:10.1016/j.actaastro.2015.04.012.
- [42] Lucchesi, D. M. et al. (2017), The LARASE research program. State of the art on Modelling and Measurements of General Relativity effects in the field of the Earth: a preliminary measurement of the Lense-Thirring effect, *Proceedings of the 2017 IEEE International Workshop on Metrology for AeroSpace*, 21-23 June, Padua, Italy.
- [43] Andrés, J. I., R. Noomen, G. Bianco, D. G. Currie, and T. Otsubo (2004), Spin axis behavior of the LAGEOS satellites, *Journal of Geophysical Research*, 109(B6), 501, doi:10.1029/2003JB002692.
- [44] Visco, M., and D. M. Lucchesi (2016), Review and critical analysis of mass and moments of inertia of the LAGEOS and LAGEOS II satellites for the LARASE program, *Advances in Space Research*, 57(9), 1928-1938, doi:10.1016/j.asr.2016.02.006.
- [45] Wilson, R. A. (1961), Rotational Magnetodynamics and Steering of Space Vehicles, Technical Report, NASA TN D-566.
- [46] Crenshaw, J. W., and P. M. Fitzpatrick (1968), Gravity Effects on the Rotational Motion of a Uniaxial Artificial Satellite, *AIAA Journal*, 6, 2140-2145.
- [47] Holland, R. L., and H. J. Sperling (1969), A First-Order Theory for the Rotational Motion of a Triaxial Rigid Body Orbiting an Oblate Primary, *The Astronomical Journal*, 74, 490-496.
- [48] Kucharski, D., T. Otsubo, G. Kirchner, and G. Bianco (2012), Spin rate and spin axis orientation of LARES spectrally determined from Satellite Laser Ranging data, *Advances in Space Research*, 50(11), 1473-1477, doi:10.1016/j.asr.2012.07.018.
- [49] Hashimoto, H., et al. (2012), Japanese Geodetic Satellite AJISAI: development, observation and scientific contributions to geodesy, *Journal of the Geodetic Society of Japan*, 58(1), 9-25.
- [50] Kucharski, D., Lim, H.-C., Kirchner, G., Otsubo, T., Bianco, G. et al. (2013), Modeling spin parameters of Ajisai, LARES and the other geodetic satellites with SLR data, *Proceedings of the 18th International Workshop on Laser Ranging*, 11-15 November, Fujiyoshida, Japan.